Simulation of wave propagation along fluid-filled cracks using high-order summation-by-parts operators and implicit-explicit time stepping [*]

OSSIAN OREILLY[§†], ERIC M. DUNHAM[†‡], AND JAN NORDSTRÖM [§]

Abstract. We present an efficient, implicit-explicit numerical method for wave propagation in solids containing fluid-filled cracks, motivated by applications in geophysical imaging of fractured oil/gas reservoirs and aquifers, volcanology, and mechanical engineering. We couple the elastic wave equation in the solid to an approximation of the linearized, compressible Navier-Stokes equations in curved and possibly branching cracks. The approximate fluid model, similar to the widely used lubrication model but accounting for fluid inertia and compressibility, exploits the narrowness of the crack relative to wavelengths of interest. The governing equations are spatially discretized using high-order summation-by-parts finite difference operators and the fluid-solid coupling conditions are weakly enforced, leading to a provably stable scheme.

Stiffness of the semi-discrete equations can arise from the enforcement of coupling conditions, fluid compressibility, and diffusion operators required to capture viscous boundary layers near the crack walls. An implicit-explicit Runge-Kutta scheme is used for time stepping and the entire system of equations can be advanced in time with high-order accuracy using the maximum stable time step determined solely by the standard CFL restriction for wave propagation, irrespective of the crack geometry and fluid viscosity. The fluid approximation leads to a sparse block structure for the implicit system, such that the additional computational cost of the fluid is small relative to the explicit elastic update. Convergence tests verify high-order accuracy; additional simulations demonstrate applicability of the method to studies of wave propagation in and around branching hydraulic fractures.

Key words. Fluid-filled crack, wave propagation, summation-by-parts, high-order accuracy, implicit-explicit.

AMS subject classifications.

1. Introduction. There is considerable interest in wave propagation in solids containing fluid-filled cracks. Hydrocarbon reservoirs, enhanced geothermal systems, and groundwater aquifers all feature fractured rock masses saturated in fluid. Fractures, or cracks, in these systems are either naturally occurring or created in hydraulic fracturing treatments, and can be as narrow as $\sim$0.1–10 mm but with lengths exceeding $\sim$100 m. Similarly high-aspect ratio cracks occur at a much larger scale in the form of magma-filled cracks known as dikes and sills, a primary component of active volcanic systems, and water-filled crevasses and basal hydraulic fractures in ice sheets and glaciers. Seismic imaging of these systems provides key constraints on the crack geometry and mechanical properties of the fluids and solids.

Simulation of wave propagation in and around fluid-filled cracks presents several computational challenges. Many of these arise from the extreme narrowness of the crack relative to wavelengths of interest; the dimensionless ratio of these two length scales is typically $\sim 10^{-3}$ or even less. Direct solution of the elastic wave equation in the solid and linearized compressible Navier-Stokes equation in the fluid, using finite difference, finite element, or discontinuous Galerkin methods, would involve either distorted meshes or very fine grid spacings that might lead to overly restrictive sta-

bility constraints for explicit time stepping and/or poorly conditioned linear systems for implicit time integration of viscous terms. Some studies have taken this direct approach, most commonly by neglecting fluid viscosity and instead using the acoustic wave equation for the fluid [32, 16, 47, 31]. Boundary element and boundary integral methods [10, 39, 48] or even hybrid boundary element / finite difference methods [6] overcome many of these issues, but are thus far restricted to inviscid fluids. Viscosity was added recently in two-dimensional finite element models by Frehner and Schmalholz [14], who solved the full linearized Navier-Stokes equation for the fluid using an unstructured mesh and a fully implicit Newmark time-stepping scheme. While a fully implicit time-stepping scheme is feasible for two-dimensional problems of moderate size, it likely becomes impractical or at least highly inefficient for three-dimensional problems. Nevertheless, their work demonstrates the key role that viscosity plays in damping waves.

Others have taken advantage of the narrowness of the crack by utilizing approximate fluid models. In these models, the crack, from the perspective of the solid, is an infinitesimally thin interface. Along this interface, a lower-dimensional set of partial differential equations (PDE) or even local relations between tractions and displacement discontinuities are used to describe the fluid response. The local relations can be as simple as traction-free interface conditions [31] though more widely adopted is the linear slip model [9]. While local relations can be incorporated into explicit elastic wave propagation codes [9, 47, 31] with relative ease, they fail to capture a fundamental type of guided wave that propagates along fluid-filled cracks. This wave, known as a Krauklis wave [24, 13, 21], has generated considerable interest in volcanology [13] and the oil and gas industry [21] because Krauklis wave resonance can be used to deduce crack geometry and properties of the fluid within the crack [27, 26].

Studies focusing on Krauklis waves have therefore utilized PDE fluid models [8, 7], though viscosity is typically neglected or captured by the assumption of fully developed (Poiseuille) flow. However, at the frequencies of interest, viscous dissipation can neither be ignored nor properly described by Poiseuille flow, as it reaches its maximum within boundary layers near the crack walls.

In this work, we present a numerical scheme that combines fully explicit time stepping of the elastic wave equation and a PDE fluid model based on a lubrication-type approximation to the linearized compressible Navier-Stokes equations. We use high-order summation-by-parts (SBP) finite difference operators [25, 42, 35, 44] for spatial discretization. The fluid-solid coupling conditions are weakly enforced using the simultaneous-approximation-term (SAT) penalty technique [5], and geometric complexity is handled with curvilinear, multiblock grids.

We identify several sources of stiffness in the semi-discrete problem, arising from compressibility and viscosity of the fluid. This stiffness is isolated by partitioning the semi-discrete equations, and advancing the partitioned system in time with a high-order implicit-explicit (IMEX) Runge-Kutta method [1, 4, 20, 36]. Similar partitioning has been exploited in related fluid-structure interaction simulations [38, 12, 29, 17, 19, 46, 15]. A major advantage of our approximate fluid model, over the full linearized Navier-Stokes equations, is that the linear system arising in the implicit component of the time-stepping scheme has a sparse block diagonal structure. This substantially enhances computational efficiency.

This paper is structured as follows. In Section 2 we describe the overall problem, with focus in 2.1 and 2.2 on the solid and fluid equations. These are combined, in 2.3, through the fluid-solid coupling conditions. These conditions are incorporated into a variational formulation of the continuous problem with a weak enforcement of coupling

conditions. We establish well-posedness by deriving an energy estimate. In Section 3 we present the semi-discrete approximation and establish stability by deriving a discrete energy estimate. In Section 4 we present the fully discrete approximation by discretizing in time using a high-order IMEX Runge-Kutta method. Section 5 demonstrates high-order convergence of the method using the method of manufactured solutions, followed by two application problems illustrating wave propagation in and around a branching fluid-filled crack. In Section 6 we provide a summary of the results and perspectives on future work.

2. Continuous problem. In this section we introduce the governing equations for the solid and fluid, along with conditions for coupling the solid and fluid across the moving crack walls. We restrict attention to the two-dimensional problem, as shown in Figure 1. The solid occupies the domain Ω_s and contains a crack, which is treated from the perspective of the solid as an infinitesimally thin interface $\Gamma \subseteq \Omega_s$. The crack contains a compressible, viscous fluid defined on the domain Ω_f. Rather than solving the compressible Navier-Stokes equations in their most general form, we seek a linearized description of the fluid, assuming small perturbations about a state of rest. Furthermore, we utilize a lubrication-type approximation to take advantage of the fact that the crack width is much smaller than wavelengths of interest; however, we retain essential terms in the linearized Navier-Stokes equations that account for fluid compressibility and inertia. Our model generalizes the model of [27] to account for crack curvature and nonplanarity of the crack walls. Similar compressible lubrication models are used in engineering, particularly for problems involving gas-filled bearings and in studies of liquid droplet impact on surfaces [45, 41, 3, 18, 2].

2.1. Solid. Assuming linear elastic material response and small strains and rotations, the solid is governed by the elastic wave equation:

$$(1) \qquad \rho_s \frac{\partial v}{\partial t} = A_x \frac{\partial \sigma}{\partial x} + A_y \frac{\partial \sigma}{\partial y},$$

$$(2) \qquad S \frac{\partial \sigma}{\partial t} = A_x^T \frac{\partial v}{\partial x} + A_y^T \frac{\partial v}{\partial y},$$

where

$$A_x = \begin{bmatrix} 1 & 0 & 0 \\ 0 & 0 & 1 \end{bmatrix}, \ A_y = \begin{bmatrix} 0 & 0 & 1 \\ 0 & 1 & 0 \end{bmatrix},$$

$v(x, y, t) = [v_x \ v_y]^T$ is the particle velocity, $\sigma(x, y, t) = [\sigma_{xx} \ \sigma_{yy} \ \sigma_{xy}]^T$ is the stress, ρ_s is the density, and $S = S^T > 0 \in \mathbb{R}^{3 \times 3}$ is the compliance matrix. Note that the x and y subscripts denote the components of the solid velocity and stress and should not be confused with partial derivatives. For an isotropic solid, as used in all simulations in this work, the compliance matrix is

$$S = \frac{G}{2} \begin{bmatrix} 1 - \nu & 0 & -\nu \\ 0 & 2 & 0 \\ -\nu & 0 & 1 - \nu \end{bmatrix},$$

where $G > 0$ is the shear modulus and $-1 < \nu < 0.5$ is Poisson's ratio. However, the numerical scheme developed below is applicable to anisotropic linear elastic solids as well.

Curvature of the crack and possibly other geometric complexities in the shape of the solid are handled by formulating the elastic wave equation in curvilinear coordinates. We also utilize a particular splitting of the equations that facilitates the
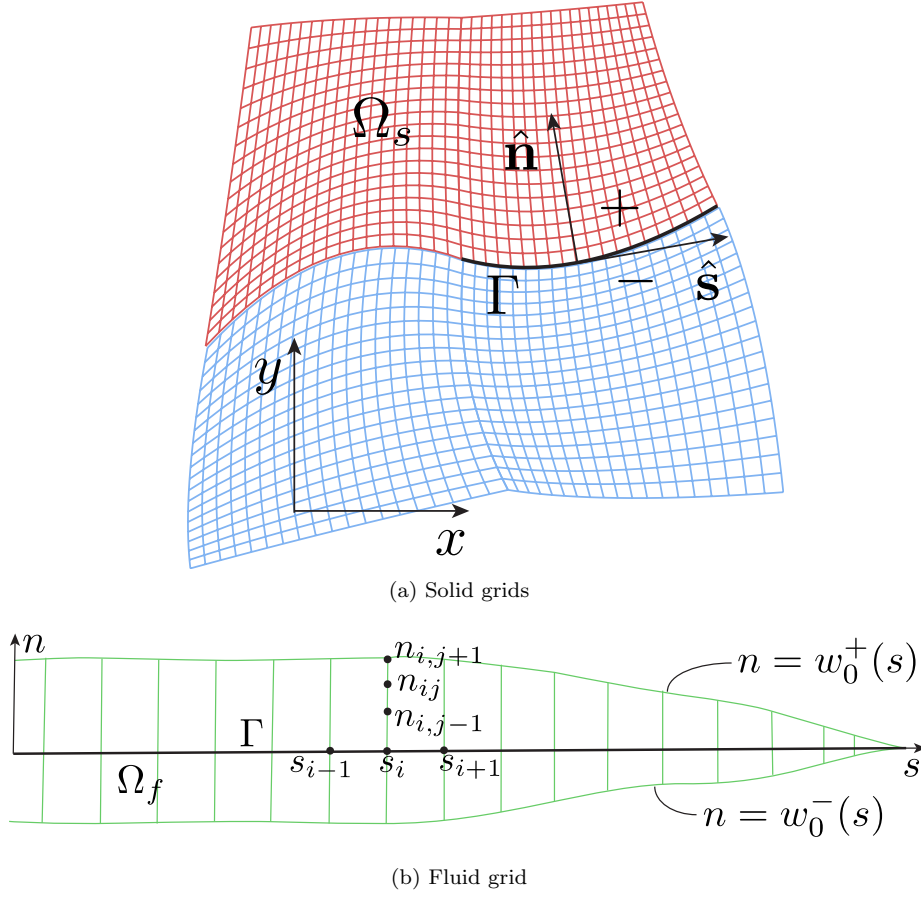
(a) Solid grids

(b) Fluid grid

FIG. 1. *(a) Linear elastic solid Ω_s containing a fluid-filled crack, appearing from the perspective of the solid as an infinitesimally thin interface Γ. $\hat{s}$ and $\hat{n}$ denote unit vectors parallel and normal to Γ, with $\hat{n}$ pointing from the $-$ side to $+$ side of Γ. (b) Zoomed-in view of the fluid domain Ω_f within the crack, along with the mesh used to resolve viscous boundary layers near the crack walls. The arc length along the crack is s and the distance across the crack width, normal to s, is n.*

construction of the semi-discrete approximation in a manner that leads to an energy estimate and thus stability [33]. Consider the curvilinear coordinate transformation $x = x(q, r), y = y(q, r) \leftrightarrow q = q(x, y), r = r(x, y)$, mapping $(x, y) \in \Omega_s$ to $(q, r) \in \widetilde{\Omega}_s$. We assume a smooth, one-to-one mapping, and define $\widetilde{\Omega}_s = [0, 1] \times [0, 1]$ as the reference unit square. Following [11], we transform the elastic wave equation by writing (1) in conservative form and (2) in non-conservative form [28], which leads to

$$(3) \qquad \rho_s J \frac{\partial v}{\partial t} = \frac{\partial}{\partial q}(J A_q \sigma) + \frac{\partial}{\partial r}(J A_r \sigma), \ S \frac{\partial \sigma}{\partial t} = A_q^T \frac{\partial v}{\partial q} + A_r^T \frac{\partial v}{\partial r},$$

where

$$(4) \qquad A_q = \begin{bmatrix} q_x & 0 & q_y \\ 0 & q_y & q_x \end{bmatrix}, \ A_r = \begin{bmatrix} r_x & 0 & r_y \\ 0 & r_y & r_x \end{bmatrix}.$$

In (4), the metric coefficients q_x, q_y, ..., are obtained by taking partial derivatives of each coordinate. For example, $q_x = \partial q / \partial x$. The metric coefficients are the only

quantities which use compact derivative notation, and should not be confused with the x and y components of a vector. Furthermore, $J > 0$ is the Jacobian of the mapping, defined as $J = x_q y_r - y_q x_r$. The metric coefficients satisfy the metric relations $Jq_x = y_r$, $Jr_x = -y_q$, $Jq_y = -x_r$, $Jr_y = x_q$.

The coupling conditions will be stated using the solid fields locally oriented with respect to the curved fluid-solid interface. We therefore define the velocity V and traction T expressed in terms of the normal and tangential components given by the unit normal $\hat{n}$ and unit tangent $\hat{s}$ along Γ (Figure 1a). We have

$$(5) \qquad V = [v_n \ v_s]^T = R^T v \quad \text{and} \quad T = [\sigma_n \ \sigma_s]^T = R^T \frac{A_r}{|\nabla r|} \sigma,$$

where v_n and v_s are the normal and tangential components of the solid particle velocity, respectively, and σ_n and σ_s are the normal and shear components of the solid traction, respectively. To obtain these components, we have introduced the rotation matrix R:

$$(6) \qquad R^T = \begin{bmatrix} \hat{n}^T \\ \hat{s}^T \end{bmatrix} = \frac{1}{|\nabla r|} \begin{bmatrix} r_x & r_y \\ r_y & -r_x \end{bmatrix},$$

where $|\nabla r| = (r_x^2 + r_y^2)^{1/2}$.

2.2. Fluid. The fluid is governed by an approximation to the linearized compressible Navier-Stokes equations. It has density ρ_f, dynamic viscosity μ, and bulk modulus K_f. The fluid equations are stated in a coordinate system (s, n) locally oriented with respect to Γ, for which s is the arc length along Γ and n measures the distance across the width of the crack in the direction normal to s. The upper and lower crack walls are initially located at $n = w_0^{\pm}(s)$ (Figure 1b), but are perturbed to $n = w^{\pm}(s, t)$. The initial width of the crack is defined as $w_0 = w_0^+(s) - w_0^-(s)$.

Following the usual procedure for deriving lubrication-type approximations [41, 3, 18], a scaling analysis of the momentum balance in the n-direction establishes uniformity of the fluid pressure across the width of the crack. Conservation of fluid mass, together with a barotropic equation of state, leads to the first governing equation for the fluid. The linearized version of this equation is, on Γ,

$$(7) \qquad \frac{w_0}{K_f} \frac{\partial p}{\partial t} + \frac{\partial}{\partial s}(w_0 \bar{u}) = -\left(\frac{\partial w^+}{\partial t} - \frac{\partial w^-}{\partial t} \right),$$

for pressure $p(s, t)$ and width-averaged velocity

$$(8) \qquad \bar{u}(s, t) = \frac{1}{w_0} \int_{w_0^-}^{w_0^+} u(s, n, t) dn,$$

where $u = u(s, n, t)$ is the fluid velocity in the s-direction. Equation (7) is derived by integrating the local form of the continuity equation across the crack width, using the kinematic condition to replace the normal component of fluid velocity with the crack opening rate, and linearizing about a state of rest.

At this point, the classical lubrication model would neglect inertia by assuming a fully developed Poiseuille flow profile, for which

$$(9) \qquad \bar{u} = \frac{w_0^2}{12\mu} \left(-\frac{\partial p}{\partial s} \right) + \frac{v_s^+ - v_s^-}{2}$$

where $v_s^+ - v_s^-$ is the discontinuity in the tangential component of solid particle velocity across Γ. However, at the frequencies of interest to us, fluid inertia leads to non-parabolic velocity profiles with Stokes-type boundary layers adjacent to the crack walls [3]. To obtain a physically relevant $\bar{u}$ we must therefore solve the s-momentum balance on the two-dimensional domain Ω_f:

$$(10) \qquad \rho_f \frac{\partial u}{\partial t} + \frac{\partial p}{\partial s} = \frac{\partial \tau}{\partial n},$$

where

$$(11) \qquad \tau = \mu \frac{\partial u}{\partial n}.$$

is the shear stress. Equation (10) retains, on the right-hand side, a single viscous term describing shearing on planes parallel to Γ and diffusive momentum transport across these planes. Effects of curvature have been neglected in the momentum balance, under the assumption that the radius of curvature of Γ is comparable to or larger than the wavelengths of interest. Note that when inertia is neglected, the solution to the momentum balance equation (10) with no-slip conditions on the crack walls provides the classical lubrication solution (9). In this classical lubrication limit, the associated shear stress on the top and bottom crack walls is

$$(12) \qquad \tau^\pm = \mp \frac{w_0}{2} \left(-\frac{\partial p}{\partial s} \right) + \frac{\mu(v_s^+ - v_s^-)}{w_0}.$$

Note that while the method developed in this paper uses the more general lubrication model that accounts for fluid inertia, it would be a straightforward extension to instead use the classical lubrication model embodied in equations (9) and (12).

We apply a coordinate transformation in the s direction for compatibility with the curvilinear grid used in the solid. We also apply a coordinate transformation in the n direction in the fluid to resolve the boundary layers by clustering grid points near the walls. Consider the coordinate transformation $s = s(q), n = n(q,r) \leftrightarrow q = q(s), r = r(s,n)$ that maps $(s,n) \in \Omega_f$ to a reference unit square $\tilde{\Omega}_f = [0, 1] \times [0, 1]$. Note that since s is the arc length of Γ, it can only depend on q. The Jacobian and metric relations become $J = s_q n_r$, $s_r = 0$, $Jq_s = n_r$, $Jr_s = -n_q$, $Jq_n = 0$, $Jr_n = s_q$. Transforming (7), (8), (10), and (11) leads to the final governing equations for the fluid:

$$(13) \qquad \begin{aligned} s_q \frac{w_0}{K_f} \frac{\partial p}{\partial t} + \frac{\partial}{\partial q}(w_0 \bar{u}) &= -s_q \left(\frac{\partial w^+}{\partial t} - \frac{\partial w^-}{\partial t} \right), \\ \rho_f J \frac{\partial u}{\partial t} + n_r \frac{\partial p}{\partial q} &= s_q \frac{\partial \tau}{\partial r}, \\ \bar{u}(q,t) &= \frac{1}{w_0} \int_{r=0}^{r=1} u(q,r,t) n_r dr, \\ \tau &= \mu r_n \frac{\partial u}{\partial r}. \end{aligned}$$

2.3. Fluid-solid coupling conditions and well-posedness. Having made several approximations, we must verify that our problem is well-posed. Well-posedness is established by enforcing the fluid-solid coupling conditions such that the governing equations satisfy a mechanical energy balance. In this analysis, we weakly enforce

230   the coupling conditions. This procedure simplifies the proof of stability in the semi-
231   discrete case, following later.

232   For simplicity, we consider only the $+$ side of the interface Γ; the $-$ side is treated
233   in an analogous manner, and boundary conditions on the solid have been discussed
234   extensively in previous work [22, 23, 11]. Since the fluid mass balance is stated on Γ,
235   we only consider the term $\partial w^+/\partial t$ in (13), which will be coupled to the solid on the
236    $+$ side. To simplify the notation in this section, we drop the $+$ superscript.

237   The fluid-solid coupling conditions for a viscous fluid are obtained by balancing
238   the tractions across the interface and enforcing the kinematic condition and no-slip
239   condition to ensure that the fluid and solid remain in contact at the crack walls:

240   (14) $$V = [v_n \ v_s]^T = \left[\frac{\partial w}{\partial t} \ u\right]^T \quad \text{and} \quad T = [\sigma_n \ \sigma_s]^T = [-p \ \tau]^T.$$
241

242   The negative sign on fluid pressure arises because pressure is positive in compression,
243   the opposite of the sign convention for solid normal stresses.

244   There are many ways in which the coupling conditions (14) can be enforced. One
245   approach is to weakly enforce a common interface velocity $\hat{V} = [\hat{V}_n \ \hat{V}_s]^T$ on the fluid
246   and solid velocities, and a common interface traction $\hat{T} = [\hat{T}_n \ \hat{T}_s]^T$ on the fluid and
247   solid tractions. This procedure uses the fact that the fluid velocities, solid velocities,
248   and tractions are continuous.   The interface velocity and traction are determined
249   by satisfying the proper mechanical energy balance of the overall problem.   In the
250   limit when the coupling conditions become strongly enforced, the fluid and solid
251   velocities and tractions should be equal to the interface velocity and traction, i.e.,
252    $\hat{V} = [v_n \ v_s]^T = [\partial w/\partial t \ u]^T$ and $\hat{T} = [\sigma_n \ \sigma_s]^T = [-p \ \tau]^T$.

253   Since our governing equations are formulated in curvilinear coordinates, we state
254   all integrations with area and length differentials in the curved domain.   The rela-
255   tionship between the area differential in the curved domain and transformed domain
256   is $d\Omega \leftrightarrow J dq dr$.   Furthermore, the relationship between the line differential for the
257   interface Γ in the curved domain and transformed domain is $ds \leftrightarrow J|\nabla r| dq$.

258   To obtain the mechanical energy balance satisfied by the fluid and solid, we
259   consider the following variational form of the solid:

(15)
$$\int_{\Omega_s} \phi_s^T \rho \frac{\partial v}{\partial t} d\Omega = \int_{\Omega_s} \phi_s^T \frac{1}{J}\frac{\partial}{\partial q}(JA_q\sigma) + \phi_s^T \frac{1}{J}\frac{\partial}{\partial r}(JA_r\sigma) d\Omega + \int_\Gamma (R^T\phi_s)^T(T-\hat{T})ds$$

$$\int_{\Omega_s} \varphi_s^T S \frac{\partial \sigma}{\partial t} d\Omega = \int_{\Omega_s} \varphi_s^T A_q^T \frac{\partial v}{\partial q} + \varphi_s^T A_r^T \frac{\partial v}{\partial r} d\Omega + \int_\Gamma \frac{(R^T A_r \varphi_s)^T}{|\nabla r|}(V-\hat{V})ds.$$

262   for smooth, vector-valued test functions $\phi_s, \varphi_s \in L^2(\Omega_s)$. In (15), the integrals along
263   the interface Γ are penalty terms, which weakly enforce the coupling conditions. The
264   rotation matrix R is defined in (6) and arises because the coupling conditions are
265   stated in terms of normal and tangential components.   One can derive the penalty
266   terms by applying integration by parts to the corresponding volume terms. Another
267   possibility is to introduce an unknown weight Σ in the penalty term and then deter-
268   mine this weight by satisfying the energy balance [34].

The fluid variational formulation is

$$
\int_{\Gamma} \phi_f \frac{w_0}{K_f} \frac{\partial p}{\partial t} + q_s \phi_f \frac{\partial}{\partial q}(\bar{u}w_0)ds = -\int_{\Gamma} \phi_f \frac{\partial w}{\partial t}ds
$$

(16)
$$
\int_{\Omega_f} \varphi_f \rho_f \frac{\partial u}{\partial t} + \varphi_f q_s \frac{\partial p}{\partial q}d\Omega = \int r_n \varphi_f \frac{\partial \tau}{\partial r}d\Omega
$$

$$
- \int_{\Gamma} \varphi_f(\tau - \hat{T}_s) + \mu r_n \frac{\partial \varphi_f}{\partial r}(u - \hat{V}_s)ds,
$$

for smooth, scalar test functions $\phi_f \in L^2(\Gamma)$ and $\varphi_f \in L^2(\Omega_f)$.

Next, we determine $\hat{V}$ and $\hat{T}$ such that the overall problem satisfies the proper mechanical energy balance. The choice of $\hat{V}$ and $\hat{T}$ resulting in well-posedness is specified in the following proposition.

PROPOSITION 1. *The fluid-solid problem (15) and (16) is well-posed and consistent with the coupling conditions (14) if $\hat{V}$ and $\hat{T}$ are chosen as the linear combinations*

(17)
$$
\hat{V} = \left[v_n + \frac{\sigma_n + p}{\alpha_n}, \ \frac{\beta_s u + \alpha_s v_s}{\alpha_s + \beta_s} + \frac{\sigma_s - \tau}{\alpha_s + \beta_s} \right]^T ,
$$

$$
\hat{T} = \left[-p, \ \frac{\alpha_s \beta_s}{\alpha_s + \beta_s}(v_s - u) + \frac{\beta_s \sigma_s + \tau \alpha_s}{\alpha_s + \beta_s} \right]^T ,
$$

for $\{\alpha_n, \alpha_s, \beta_s > 0\} \cup \{\alpha_s = 0, \ \beta_s > 0\} \cup \{\beta_s = 0, \ \alpha_s > 0\}$.

Proof. By choosing test functions $\phi_s = v$, $\varphi_s = \sigma$, $\phi_f = p$, $\varphi_f = u$ in (15) and (16), combining terms, and integrating by parts, we find

$$
\frac{dE}{dt} + \Phi = -\int_{\Gamma} \left(v_n \sigma_n + v_s \sigma_s - v_n(\sigma_n - \hat{T}_n) - v_s(\sigma_s - \hat{T}_s) \right.
$$

$$
\left. - \sigma_n(v_n - \hat{V}_n) - \sigma_s(v_s - \hat{V}_s) \right)ds
$$

$$
- \int_{\Gamma} p\frac{\partial w}{\partial t} - \tau u + u(\tau - \hat{T}_s) + \tau(u - \hat{V}_s)ds.
$$

In (1), $\Phi = \int_{\Omega_f} \tau^2/\mu d\Omega \geq 0$ is the viscous energy dissipation rate and, E is the mechanical energy

(18)
$$
E = \frac{1}{2}\int_{\Omega_s} \rho_s v^T v + \sigma^T S\sigma d\Omega + \frac{1}{2}\int_{\Gamma} \frac{w_0}{K_f}p^2 ds + \frac{1}{2}\int_{\Omega_f} \rho_f u^2 d\Omega,
$$

where the respective terms are the kinetic and strain energy in the solid, and the elastic and kinetic energy in the fluid.

Next, we add and subtract $\hat{T}_n\hat{V}_n$ and $\hat{T}_s\hat{V}_s$ to the right-hand side of (1), which after some algebra leads to

(19)
$$
\frac{dE}{dt} + \Phi = -\int_{\Gamma} \hat{T}_n\hat{V}_n + \hat{T}_s\hat{V}_s - (\sigma_n - \hat{T}_n)(v_n - \hat{V}_n) - (\sigma_s - \hat{T}_s)(v_s - \hat{V}_s)ds
$$

$$
- \int_{\Gamma} p\frac{\partial w}{\partial t} - \hat{T}_s\hat{V}_s + (u - \hat{V}_s)(\tau - \hat{T}_s)ds.
$$

$$
= -(\mathcal{P} + \mathcal{R}),
$$

295 where

296 (20) $$\mathcal{P} = \int_\Gamma \hat{T}_n \hat{V}_n + p \frac{\partial w}{\partial t} ds,$$

297
298 (21) $$\mathcal{R} = \int_\Gamma (u - \hat{V}_s)(\tau - \hat{T}_s) - (\sigma_n - \hat{T}_n)(v_n - \hat{V}_n) - (\sigma_s - \hat{T}_s)(v_s - \hat{V}_s) ds.$$

299 In (19), we have partitioned the right-hand side into two terms: $\mathcal{P}$ and $\mathcal{R}$. The first
300 term $\mathcal{P}$ contains the flow of energy from the fluid to the solid and vice versa. When
301 the coupling conditions are enforced, this term must vanish. The second term $\mathcal{R}$ is a
302 residual term arising due to the weak enforcement of the coupling conditions. This
303 term needs to be non-negative and to vanish when the coupling conditions are exactly
304 satisfied. To obtain a well-posed problem, we therefore need to choose $\hat{V}$ and $\hat{T}$ such
305 that $\mathcal{P} = 0$ and $\mathcal{R} \geq 0$. By choosing

306
307 (22) $$\hat{T}_n = -p \quad \text{and} \quad \hat{V}_n = \frac{\partial w}{\partial t},$$

308 we obtain $\mathcal{P} = 0$. To bound $\mathcal{R}$, consider the choice

309
310 (23) $$\sigma_n - \hat{T}_n = -\alpha_n(v_n - \hat{V}_n), \ \sigma_s - \hat{T}_s \ = -\alpha_s(v_s - \hat{V}_s), \ \tau - \hat{T}_s = \beta_s(u - \hat{V}_s),$$

311 for penalty parameters $\alpha_n, \alpha_s, \beta_f \geq 0$. Guidelines for choosing these penalty param-
312 eters are given later. Then (21) becomes

313
314 $$\mathcal{R} = \int_\Gamma \alpha_n(v_n - \hat{V}_n)^2 + \alpha_n(v_s - \hat{V}_s)^2 + \beta_s(u - \hat{V}_s)^2 \geq 0.$$

315 By inserting (22) and (23) into (19), we obtain the bound

316
317 $$\frac{dE}{dt} = -\Phi - \mathcal{R} \leq 0.$$

318 Note that $\mathcal{R}$ vanishes when the coupling conditions are satisfied exactly, and the
319 energy balance in this limit exactly coincides with the correct mechanical energy
320 balance (i.e., $dE/dt = -\Phi \leq 0$).
321 When implementing this scheme, we need to determine $\hat{V}$ and $\hat{T}$. This is done
322 by solving (22) and (23) for $\hat{V}$ and $\hat{T}$, which yields the stated solution (17). Finally,
323 to show that (17) is consistent with (14), insert (17) into the variational formulations
324 (15) and (16). □

325 **3. Semi-discrete approximation.** In this section, we utilize the results estab-
326 lished in the previous section to construct a stable, semi-discrete approximation. We
327 closely follow the continuous analysis by formulating the semi-discrete approximation
328 in variational form. This will be done by using SBP operators, which are necessary
329 for obtaining a discrete energy estimate and hence a proof of stability.

330 **3.1. Definitions.** While a multiblock discretization is used for both the fluid
331 and solid domains in realistic applications, we keep the presentation brief by focusing
332 on only one solid and one fluid block. The solid block is located above the crack, as
333 illustrated in Figure 1a. Let the reference domain $\hat{\Omega} = [0, 1] \times [0, 1]$ be discretized
334 by an $(N_q + 1) \times (N_r + 1)$ two-dimensional grid. Furthermore, let the two coordinate
335 directions q and r in the reference domain be discretized by $q_i = i\Delta q$ for $0 \leq i \leq N_q$,
336 and $r_j = j\Delta r$ for $0 \leq j \leq N_r$ using grid spacings $\Delta q = 1/N_q$ and $\Delta r = 1/N_r$. For

each field, we introduce a grid function $u_{ij}(t) = u(q_i, r_j, t)$, which is stored in a vector $u(t)$ with r being the contiguous direction. The storage order of u_{ij} is, of course, arbitrary, but our particular choice facilitates organization and presentation through use of Kronecker tensor product notation.

Having introduced grids and grid functions, next we define SBP operators. An SBP first derivative difference operator is given in Definition 1; its properties are satisfied by construction.

DEFINITION 1. *The difference operator D is a summation-by-parts first derivative SBP(2s,s) with interior accuracy 2s and boundary accuracy s with following properties.*

1. *The diagonal matrix $H > 0$ defines the discrete norm*

$$(24) \qquad \|\phi\|_h^2 = \phi^T H \phi, \ \|\phi\|_h^2 \approx \|\phi\|^2 = \int_0^1 \phi^2 dx,$$

for a smooth test function ϕ and a corresponding grid function ϕ.

2. *The SBP property*

$$(25) \qquad HD + D^T H = B = diag([-1 \ 0 \ \dots \ 1])$$

holds. Here, B is the restriction of ϕ to the right and left boundary:

$$\phi^T B \phi = \phi_N^2 - \phi_0^2.$$

For more details concerning accuracy relations, see [42, **?**].

3.2. Solid. By using the definition of the SBP difference operator, we discretize the variational formulation of the solid (15):

$$(26)$$

$$\phi_s^T (I_2 \otimes \rho M_s) \frac{dv}{dt} = \phi_s^T (I_2 \otimes M_s J^{-1}) \big((I_2 \otimes D_q \otimes I_r)(I_2 \otimes J) A_q$$
$$+ (I_2 \otimes I_q \otimes D_r)(I_2 \otimes J) A_r) \sigma + (R^T L_s^T \phi_s)^T (I_2 \otimes \bar{M}_s)(T - \hat{T}),$$

$$\varphi_s^T S(I_3 \otimes M_s) \frac{d\sigma}{dt} = \varphi_s^T (I_3 \otimes M_s) \big(A_q^T (I_3 \otimes D_q \otimes I_r) + A_r^T (I_3 \otimes I_q \otimes D_r) \big) v$$
$$+ (I_2 \otimes |\nabla r|^{-1} R^T L_s A_r \varphi_s)^T (I_2 \otimes \bar{M}_s)(V - \hat{V}).$$

In (26), all of the material properties, Jacobian, and metric coefficients, evaluated at each grid point, are stored in diagonal matrices. The matrix I_2 is a 2×2 identity matrix, and $\otimes$ is the Kronecker product. The difference operators D_q and D_r are SBP finite difference operators (see Definition 1). The matrices A_q and A_r are block diagonal matrices containing the metric coefficients (approximated using SBP operators). In the penalty terms, the operator L_s is used to obtain the velocity V and traction T on the interface. For example, we compute V using $V = R^T L_s^T v$, where $L_s = I_2 \otimes I_q \otimes e_0$, and $e_0 = [1 \ 0 \ \dots \ 0]^T$. The rotation matrix R is defined using (6). The interface velocity $\hat{V}$ and traction $\hat{T}$, given in (17), are determined in a similar manner. The mass matrices M_s and $\bar{M}_s$ are diagonal matrices obtained by approximating integrals over Ω_s and along Γ, respectively, using the SBP quadrature rules given in Definition 1. We have $M_s = J(H_q \otimes H_r)$ and $\bar{M}_s = L^T J |\nabla r| L H_q$.

Since the variational formulation holds for all non-trivial test functions, we obtain the strong formulation of the semi-discrete approximation of the solid by eliminating the test functions in (26) and inverting the matrices on the left-hand side. Note that the strong form of the equations (26) can be directly advanced in time using explicit time stepping since the mass matrices are diagonal and the inverse of S is known.

378   **3.3. Fluid.** Many of the definitions needed to formulate the semi-discrete ap-
379   proximation of the solid equations are also used to formulate the semi-discrete ap-
380   proximation of the fluid equations. One difference, however, is the appearance of the
381   second derivative operator in the viscous diffusion term. While the second derivative
382   can be constructed by applying the first derivative twice, this procedure leads to a
383   difference operator with sub-optimal stencil width and accuracy. Therefore, in our im-
384   plementation, we use a compact second derivative operator with variable coefficients
385   [30]. However, since the presentation and proof of stability become more complicated
386   when using compact operators, in the derivation below we use the first derivative
387   applied twice.
388   The discretization of the weak form of the fluid governing equations (16) is

(27)

$$\phi_f^T \bar{M}_f \left(w_0 K_f^{-1} \frac{dp}{dt} + q_s D_q \bar{u} w_0 \right) = -\phi_f^T \bar{M}_f \frac{\partial w}{\partial t}$$

$$\varphi_f^T M_f \left(\rho_f \frac{du}{dt} + (q_s D_q p) \otimes e_r \right) = \varphi_f^T M_f r_n (I_q \otimes D_r)\tau - (L_f^T \varphi_f)^T \bar{M}_f (L_f^T \tau - \hat{T}_s)$$

$$- (L_f^T (I_q \otimes D_r)\varphi_f)^T \bar{M}_f r_n \left(L_f^T u - \hat{V}_s \right).$$

391   In (27), the shear stress τ is determined by

(28)
$$\tau = \mu n_r (I_q \otimes D_r)u.$$

394   The width-averaged velocity $\bar{u}$ is computed using the SBP quadrature rule:

(29)
$$\bar{u} = (w_0 \otimes e_r^T H_r)n_r u \approx \frac{1}{w_0} \int_{r=0}^{r=1} u n_r dr,$$

397   where $e_r = [1 \; 1 \; \dots \; 1]^T$. We approximate volume integrals over Ω_f and surface
398   integrals along Γ using $M_f = (s_q H_q \otimes H_r)n_r$ and $\bar{M}_f = H_q s_q$, respectively. Since
399   the quadrature rules along the interface on the fluid and solid sides are constructed
400   in the same way, we define $\bar{M} = \bar{M}_f = \bar{M}_s$. Note that the quadrature rule H_r, used
401   to calculate $\bar{u}$, is the same as the one constructing M_f. This is required to obtain an
402   energy balance for the semi-discrete approximation.

403   **3.4. Stability.** Finally, we show that the semi-discrete approximation is stable
404   through the following proposition.

405   PROPOSITION 2. *The fluid-solid semi-discrete approximation given by (26) and*
406   *(27) is stable.*

407   *Proof.* The results follow from Proposition 1 and use of the SBP property (25).
408   The energy (18) is approximated as

$$E_h = \frac{1}{2}v^T (I_2 \otimes \rho_s M_s)v + \frac{1}{2}\sigma^T S(I_3 \otimes M_s)\sigma + \frac{1}{2}p^T w_0 K^{-1} \bar{M}_f p + \frac{1}{2}u^T \rho_f M_f u.$$

411   The semi-discrete approximations (26) and (27) satisfy

$$\frac{dE_h}{dt} + \Phi_h = -\alpha_n (v_n - \hat{V}_n)^T \bar{M}(v_n - \hat{V}_n) - \alpha_s (v_s - \hat{V}_s)^T \bar{M}(v_s - \hat{V}_s)$$

$$- \beta_s (u - \hat{V}_s)^T \bar{M}(u - \hat{V}_s) \leq 0.$$

Here, $\Phi_h = \tau^T M_f \tau / \mu \geq 0$ approximates the viscous energy dissipation rate. Since the energy rate of the semi-discrete approximation is non-positive, the numerical solution is bounded, implying stability. The terms arising from the weak enforcement of the coupling conditions yield additional numerical dissipation, vanishing with grid refinement.   □

4. Fully discrete approximation. Next we turn our attention to time stepping. While the overall problem is dominantly one of wave propagation, there are several sources of stiffness. Our objective here is to advance the solution in time, with high-order accuracy, using a fully explicit method for the elastic wave equation (anticipating that this will dominate the computational expense) and with a time step limited only by the usual CFL condition for wave propagation. To overcome stiffness, we formulate the fully discrete scheme by first partitioning the semi-discrete approximation into stiff and non-stiff parts. The latter accounts for all terms in the governing equations describing wave propagation in the solid and fluid. Then we advance the partitioned system in time using a high-order implicit-explicit (IMEX) Runge-Kutta method [1, 4, ?, 20]. The stiff and non-stiff terms are integrated implicitly and explicitly in time, respectively.

The semi-discrete approximations (26) and (27) are written in matrix-vector form as

$$(30) \qquad \frac{dq}{dt} = Wq + Cq + g(t), \; q = \begin{bmatrix} q_f \\ q_s \end{bmatrix}, \; W = \begin{bmatrix} W_f & 0 \\ 0 & W_s \end{bmatrix}, \; C = \begin{bmatrix} C_f & C_{fs} \\ C_{sf} & C_s \end{bmatrix},$$

where $q_f = [p^T, \; u^T]^T$ and $q_s = [v^T, \; \sigma^T]^T$. In (30), the matrix W holds the difference operators and boundary terms of the fluid and solid, C holds the fluid-solid coupling terms, and $g(t)$ is a forcing function containing external data. We partition (30) into

$$(31) \qquad\qquad\qquad \frac{dq}{dt} = F^{IM}q + F^{EX}q + g(t),$$

where

$$(32) \qquad\qquad F^{IM} = \begin{bmatrix} W_f^{IM} + C_f & C_{fs} \\ 0 & 0 \end{bmatrix}, \; F^{EX} = \begin{bmatrix} W_f^{EX} & 0 \\ C_{sf} & M_s + C_s \end{bmatrix}$$

will be treated implicitly and explicitly, respectively. The partitioning of W_f treats diffusion (contained in W_f^{IM}) implicitly and wave propagation (contained in W_f^{EX}) explicitly. In this work we apply the time integrator ARK4(3)6L[2]SA-ESDIRK (implicit component) and ARK4(3)6L[2]SA-ERK (explicit component) presented in [20]. For future reference, we shall refer to this scheme as ARK4.

4.1. Choice of penalty parameters. The stiffness of the partitioned, fully discrete scheme (32) is influenced by the penalty parameters α_n, α_s, and β_s appearing in Proposition 1. We explain how to choose the parameters such that the maximum stable time step is set by the usual CFL condition for wave propagation.

To determine the maximum stable time step, we compute the spectral radius of the IMEX stability function given in [4]. This function is the iteration matrix $\widehat{R}(F^{EX}, F^{IM})$ of the fully discrete approximation

$$(33) \qquad\qquad\qquad\qquad q^{k+1} = \widehat{R}q^k,$$

with $g(t) = 0$ in (32). In (33), q^k denotes the numerical solution at time $t_k = k\Delta t$ for $k = 0, 1, 2, \ldots$, and Δt is the time step. If the spectral radius $\rho(\widehat{R}) > 1$, then

the approximation is not stable. The maximum stable time step is then defined as $\max \Delta t$ s.t. $\rho(\widehat{R}) \leq 1$ and $\widehat{R}$ is diagonalizable.

As in our previous work [22, 23, 11], the solid penalty parameters α_n and α_s are chosen to match the compressional and shear wave impedances, respectively:

$$(34) \qquad \alpha_n = Z_p = \rho_s c_p \quad \text{and} \quad \alpha_s = Z_s = \rho_s c_s,$$

where $c_p = \sqrt{M/\rho_s}$ is the compressional wave speed, with $M = 2G(1-\nu)/(1-2\nu)$, and $c_s = \sqrt{G/\rho_s}$ is the shear wave speed. We refer to this choice of penalty parameters as the characteristic choice because α_s and α_n can be obtained by solving the Riemann problem of the elastic wave equation.

The fluid penalty parameter β_s is determined by minimizing the spectral radius of the semi-discrete approximation of a one-dimensional model problem describing plane shear waves normally incident on a layer of viscous fluid. Thus, we consider the coupling of the shear wave equation to the diffusion equation in one dimension:

$$
\begin{aligned}
\int \phi_s \rho_s \frac{\partial v_x}{\partial t} dy &= \int \phi_s \frac{\partial \sigma_{xy}}{\partial y} dy + \left[\phi_s \left(\frac{\alpha_s(\sigma_{xy} - \tau)}{\alpha_s + \beta_s} - \frac{\alpha_s \beta_s}{\alpha_s + \beta_s}(v_x - u) \right) \right]_{y=0^+}, \\
(35) \quad \int \varphi_s \frac{1}{G} \frac{\partial \sigma_{xy}}{\partial t} dy &= \int \varphi_s \frac{\partial v_x}{\partial y} dy + \left[\phi_s \left(\frac{\beta_s(v_x - u)}{\alpha_s + \beta_s} - \frac{\sigma_{xy} - \tau}{\alpha_s + \beta_s} \right) \right]_{y=0^+}, \\
\int \phi_f \rho_f \frac{\partial u}{\partial t} dn &= \int \phi_f \tau \, dn - \left[\phi_f \left(\frac{\beta_s(\tau - \sigma_{xy})}{\alpha_s + \beta_s} + \frac{\alpha_s \beta_s}{\alpha_s + \beta_s}(u - v_x) \right) \right. \\
&\quad \left. + \mu \frac{\partial \phi_f}{\partial n} \left(\frac{\alpha_s(u - v_x)}{\alpha_s + \beta_s} + \frac{\tau - \sigma_{xy}}{\alpha_s + \beta_s} \right) \right]_{n=w_0^+}.
\end{aligned}
$$

In (35), the crack is located at $y = 0$ in the solid. We have weakly enforced the coupling conditions $v_x = u$ and $\sigma_{xy} = \tau$ on the top crack wall ($y = 0^+$ in the solid and $n = w_0^+$ in the fluid) using Proposition 1.

Since the penalty parameters carry units of impedance, a reasonable choice for β_s would be the fluid impedance. For a time-harmonic solution in the boundary layer limit the fluid impedance is $Z_f(\omega) = (\mu \rho_f \omega)^{1/2}$. However, since the fluid impedance depends on the angular frequency ω, we cannot use it directly. Instead, we estimate it in the following manner. Let ω^* be a frequency of interest. Then, for accuracy, we constrain the fluid and solid grid spacings to be $\Delta x_f = (\mu/\rho_f \omega^*)^{1/2}$ (to resolve the momentum diffusion length at this frequency) and $\Delta x_s = c_s/\omega^*$ (to resolve shear waves), respectively. The impedance parameter can be chosen as $\beta_s = Z_f(\omega^*) = \mu/\Delta x_f$.

While $\beta_s = \mu/\Delta x_f$ is a reasonable choice for many problems, it is not always optimal. To demonstrate this, we also investigate two alternative choices that arise in certain limits, specifically when the fluid impedance vanishes ($\beta_s = 0$, as for an inviscid fluid) or when the fluid impedance approaches infinity ($\beta_s \to \infty$). To enforce $\beta_s \to \infty$, we analytically take the limit. Then (35) becomes

$$
\begin{aligned}
\int \phi_s \rho_s \frac{\partial v_x}{\partial t} dy &= \int \phi_s \frac{\partial \sigma_{xy}}{\partial y} dy - \left[\phi_s \alpha_s (v_x - u) \right]_{y=0^+}, \\
\int \varphi_s \frac{1}{G} \frac{\partial \sigma_{xy}}{\partial t} dy &= \int \varphi_s \frac{\partial v_x}{\partial y} dy + \left[\varphi_s (v_x - u) \right]_{y=0^+}, \\
\int \phi_f \rho_f \frac{\partial u}{\partial t} dn &= \int \phi_f \tau \, dn - \left[\phi_f \left((\tau - \sigma_{xy}) + \alpha_s(u - v_x) \right) \right]_{n=w_0^+}.
\end{aligned}
$$

494   The part of parameter space that we investigate depends on the ratio of the fluid
495   impedance Z_f (in the boundary layer limit) to solid impedance Z_s:

$$\gamma = \frac{Z_f}{Z_s} = \frac{\sqrt{\mu \omega^* \rho_f}}{\rho_s c_s} = \frac{\Delta x_f \rho_f}{\Delta x_s \rho_s}.$$

498   For simplicity, we restrict attention to $\rho_s = \rho_f$ and use the SBP(6,3) operators to
499   discretize (35). For each choice of β_s, we compute the spectral radius $\rho(W + C)$
500   as a function of the impedance ratio γ (Figure 2). Here, the $W + C$ is matrix in
501   the semi-discrete approximation of (35), which can be put in the same form as (32).
502   Figure 2 shows that $\beta_s = 0$ minimizes $\rho(W + C)$ for $\gamma \ll 1$, whereas for larger values
503   of γ, $\beta_s \to \infty$ is the optimal choice. Note that for $\gamma \ll 1$, the spectral radius for
504   $\beta_s = \mu/\Delta x_f$ is nearly identical to that for $\beta_s = 0$. Therefore, in our implementation,
505   we never use $\beta_s = \mu/\Delta x_f$, because it is more complicated to implement and shows
506   no benefit compared to $\beta_s = 0$ for $\gamma \ll 1$.
507   Instead, we propose the following strategy for choosing β_s:

508   (36)
$$\beta_s = \begin{cases} 0, & \gamma < \gamma^* \\ \infty, & \gamma > \gamma^* \end{cases}.$$

510   The parameter γ^* is defined as the value of γ at which $\rho\big(W + C(\beta_s = 0)\big) = \rho\big(W +$
511   $C(\beta_s \to \infty)\big)$, as estimated from Figure 2. For the example shown, $\gamma^* \approx 10^{-1}$.
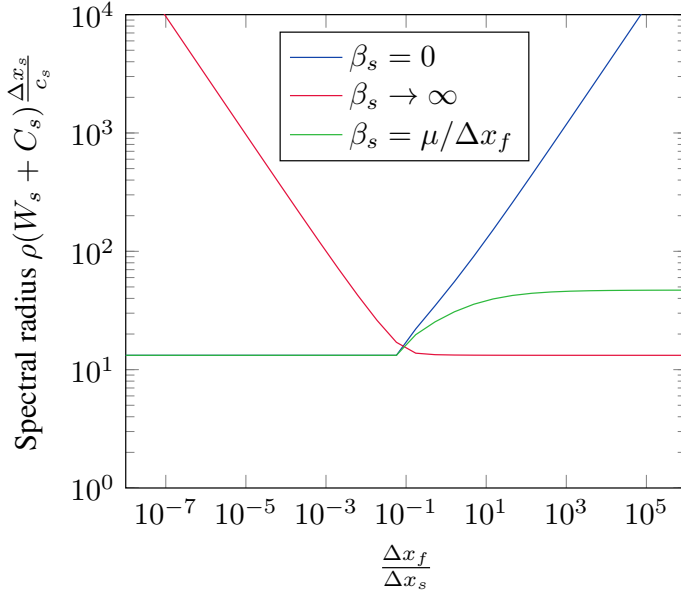

FIG. 2. *Spectral radius $\rho(W + C)$ of the semi-discrete approximation of the problem (35).*

512   Note, however, that while this choice ensures that the spectral radius of the semi-
513   discrete approximation is minimized, there is no guarantee that the fully discrete
514   approximation is stable for a time step set by the usual CFL condition for wave
515   propagation. For example, the use of energy-conserving coupling conditions, which
516   are traditionally used in many fluid-structure interaction applications, results in loss

517 of stability (see Appendix A for more details). By also analyzing the fully discrete
518 approximation, we have found that when choosing the penalty parameters as (34)
519 and (36), the maximum stable time step remains constant regardless of the amount
520 of stiffness (i.e., the time step is not restricted by the width of the fluid layer or fluid
521 properties). We have therefore achieved our objective of developing a fully discrete
522 scheme that can be advanced with a time step determined only by wave propagation.

523   **5. Numerical Experiments.** In this last part of the paper we investigate the
524 accuracy of our numerical scheme using the method of manufactured solutions and
525 showcase the code capabilities with two application problems featuring a curved,
526 branching crack.

527   **5.1. Manufactured solutions.** We construct a smooth solution and quantify
528 error and convergence rate using the method of manufactured solutions [40]. Param-
529 eters are chosen for which the semi-discrete equations are quite stiff; this provides a
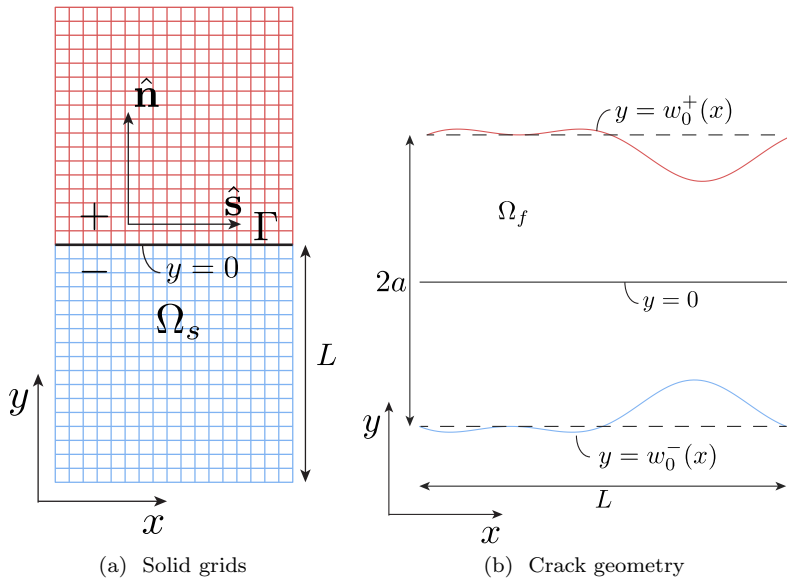530 comprehensive test of the partitioning and IMEX time-stepping procedure.

FIG. 3. *MMS verification problem. Two square blocks, Ω_1 (blue) and Ω_2 (red), are joined along the fluid-filled crack Γ, which has the nonplanar geometry shown on the right.*

531   Let the solid domain Ω_s be the rectangle $[0,\ L] \times [-L,\ L]$ with a nominally planar
532 crack Γ at $y = 0$ (see Figure 3). Since the geometry is not curved in this test, we will
533 denote all fields using Cartesian coordinates x, y. The geometry is discretized using
534 two elastic blocks (one on each side of the crack) with $(n+1) \times (n+1)$ grid points
535 and a single fluid block of size $(n+1) \times (m+1)$, where $n = 12 \times 2^j$, $m = 16 \times 2^j$, and
536 $j = 1, 2, \ldots, 5$. A manufactured solution is constructed by adding forcing functions
537 to the governing equations and boundaries and by exactly satisfying the coupling
538 conditions (14). The manufactured solution in the fluid and the crack geometry are

539   (37) $p(x,t) = \sin(kx)\cos(\omega t),\ u(x,y,t) = \sin(kx)\sin(ky)\cos(\omega t) + \sin(kx)\cos(\omega t),$

540
541   (38) $w_0^+(x) = a + b\big(1 - \sin(kx)\big)\sin(kx),\ w_0^-(x) = -a - b\big(1 - \sin(kx)\big)\sin(kx),$

a	b	ρ_f	c_0	μ	ρ_s	c_p	c_s
1 m - 0.1 mm	0.1 a	1 g/cm^3	1.5 km/s	1 mPas	2 g/cm^3	5 km/s	3 km/s

TABLE 1
Fluid and solid properties used in the MMS verification problem. The same fluid properties are used in the branching crack problem.

	$n = 24$	$n = 48$	$n = 96$	$n = 192$	$n = 384$
$\rho(M_f)/\rho(M_s)$	2.2×10^4	3.0×10^4	5.7×10^4	1.1×10^5	2.3×10^5

TABLE 2
Spectral radius ratio, a measure of stiffness for the MMS verification problem.

respectively. We prescribe the motion of the interface using

$$(39) \qquad \frac{\partial w^+(x,t)}{\partial t} = \sin(kx)\sin(\omega t), \quad \frac{\partial w^-(x,t)}{\partial t} = -\sin(kx)\sin(\omega t).$$

The manufactured solution in the solid is

$$
\begin{aligned}
v_x(x, y \geq 0^+, t) &= u(x, w_0^+, t)c(ky), & v_x(x, y \leq 0^-, t) &= u(x, w_0^-, t)c(ky), \\
v_y(x, y \geq 0^+, t) &= s(kx)s(\omega t), & v_y(x, y \leq 0^-, t) &= -s(kx)s(\omega t), \\
\sigma_{xx}(x, y \geq 0^+, t) &= c(kx)c(ky)c(\omega t), & \sigma_{xx}(x, y \leq 0^-, t) &= c(kx)c(ky)c(\omega t), \\
\sigma_{yy}(x, y \geq 0^+, t) &= -p(x,t)c(ky), & \sigma_{yy}(x, y \leq 0^-, t) &= -p(x,t)c(ky), \\
\sigma_{xy}(x, y \geq 0^+, t) &= \tau(x, w_0^+, t)c(ky), & \sigma_{xy}(x, y \leq 0^-, t) &= \tau(x, w_0^-, t)c(ky),
\end{aligned}
\tag{40}
$$

where $\tau(x,y,t) = \mu\partial u/\partial y = \mu k s(kx)c(ky)c(\omega t)$, $c(x) = \cos(x)$, $s(x) = \sin(x)$, $k = 2\pi/L$ m^{-1}, $L = 1$ m, and $\omega = 20$ s^{-1}. For the manufactured solution to satisfy the governing equations of the fluid and solid, we need to add forcing functions. These forcing functions are obtained by inserting (37)-(40) into the governing equations. To conserve space, we have omitted presenting the forcing functions. Initial conditions are determined by evaluating (37) and (40) at $t = 0$. Boundary conditions are enforced by specifying (37) and (40) as data on the incoming characteristic variable. Additional parameters are listed in Table 1. After discretizing with SBP-SAT, the semi-discrete approximation becomes stiff (Table 2).

The numerical error $e^{(n_j)} = u^{(n_j)} - u^*$ is defined as the difference of the numerical solution $u^{(n_j)}$, and the exact solution u^* sampled at the grid points of the jth grid and computed using (37) and (40). The convergence rate is

$$\text{rate} = \log_2\left(\frac{\|e^{(n_j)}\|_h}{\|e^{(n_{j+1})}\|_h}\right),$$

where $\|e^{(n_j)}\|_h$ is the norm of the error, in the energy norm on the jth grid. Time integration is carried out using ARK4 to the final time $t = 0.16$ s with a time step $\Delta t = h/c_p$, where h is the grid spacing in the solid. We test using the SBP(6,3) operators. Table 3 shows that the scheme is 4th-order accurate, confirming the expected order of accuracy [43].

5.2. Branching cracks at a material interface. Next we present two application problems featuring a curvilinear crack branching into two additional crack

		$n = 24$	$n = 48$	$n = 96$	$n = 192$	$n = 384$
$w_0 = 1$ m	$\log_{10}$ error	0.04	-1.13	-2.75	-4.27	-5.64
	rate		3.90	5.37	5.05	4.56
$w_0 = 0.1$ m	$\log_{10}$ error	-0.55	-1.83	-3.13	-4.42	-5.73
	rate		4.27	4.31	4.30	4.35
$w_0 = 1$ cm	$\log_{10}$ error	-0.63	-1.87	-3.13	-4.42	-5.73
	rate		4.11	4.21	4.29	4.35
$w_0 = 1$ mm	$\log_{10}$ error	-0.63	-1.87	-3.13	-4.42	-5.73
	rate		4.11	4.21	4.29	4.35
$w_0 = 0.1$ mm	$\log_{10}$ error	-0.63	-1.87	-3.13	-4.42	-5.73
	rate		4.12	4.21	4.29	4.34

TABLE 3
Errors and convergence rates for the MMS verification problem.

	ρ_s	G	ν	c_p	c_s
Ω_1	2.4 g/cm^3	10 GPa	0.3	3800 m/s	2000 m/s
Ω_2	2.4 g/cm^3	20 GPa	0.3	5400 m/s	2800 m/s

TABLE 4
Solid material properties for Ω_1 and Ω_2 in the branching crack problem. Compressional and shear wave speeds c_p and c_s have been computed from the density ρ_s, shear modulus G, and Poisson's ratio ν.

segments along a material interface. This geometry can arise in many natural and engineered systems (volcanoes, oil and gas reservoirs, and glaciers) due to hydraulic fracturing of material Ω_1. Continued influx of fluid causes the crack to grow through Ω_1 until it encounters a stiffer material Ω_2. The crack then branches by exploiting joints (pre-existing fractures) along the material interface. Figure 4 shows the setup. The fluid-filled crack is represented by 5 piecewise smooth and connected segments Γ_i (see Appendix 2 for coupling conditions at the crack junction). The main crack is 5 mm wide and the branches are 1 mm wide at the junction and 0.01 mm wide at the crack tips. The fluid and solid material properties are listed in Tables 1 and 4, respectively.

The computational domain is discretized using a multiblock grid (Figure 4). Boundary- and interface-conforming structured grids are generated using cubic B-splines and transfinite interpolation. The Jacobian and metric coefficients for each grid are computed using the SBP(6,3) first derivative operators. While the Jacobian is smooth inside each block, it is discontinuous across the interfaces.

We use the SBP(6,3) finite difference operators and qualitatively assess grid convergence by performing several levels of grid refinement. To advance the solution in time, we use ARK4 with a time step $\Delta t = 0.7 \times h_{min}/c_{max}$, where $c_{max} = c_p^{(2)}$ and h_{min} is the minimum grid spacing in the solid. On the coarse grid, the minimum grid spacing in the solid is $h_{min} = 1.9$ mm and in the fluid (in the n direction) it is $h_{min} = 62.5$ nm. With a fully explicit time stepping scheme we estimate that we would need to reduce the time step by at least two orders of magnitude.

Below we present results for the two problems. Both have exactly the same geometry, mesh, material properties, and boundary conditions; they differ only in how waves are excited. In both problems, the fluid and solid are initially at rest, except as indicated.

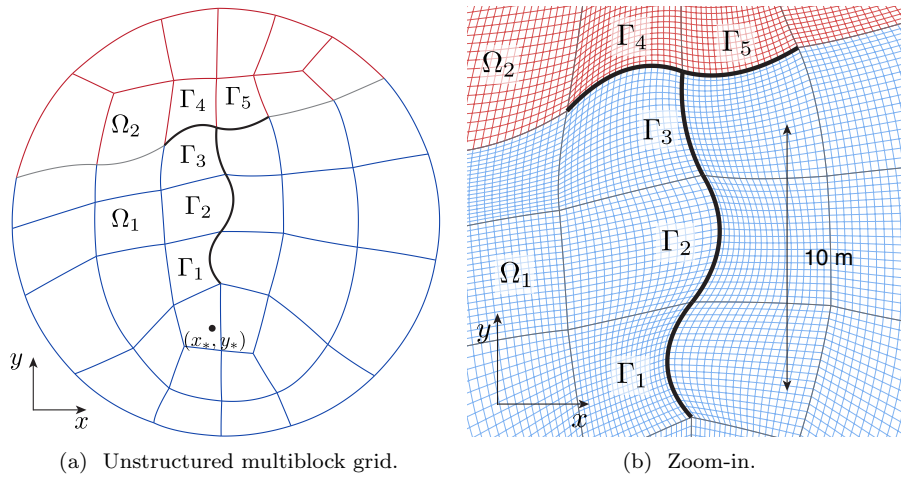(a) Unstructured multiblock grid.

(b) Zoom-in.

FIG. 4. *Geometry of branching crack problem. A fluid-filled crack Γ cuts through the solid Ω_1 (blue) before branching, at the interface with a stiffer solid Ω_2 (red), into two crack segments along the material interface.*
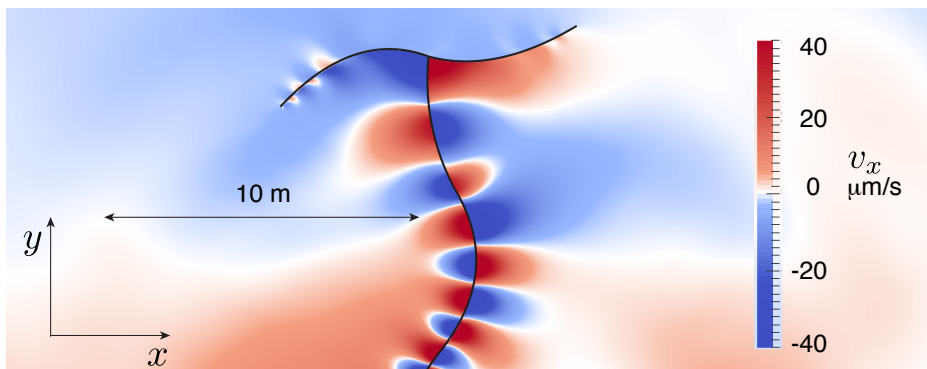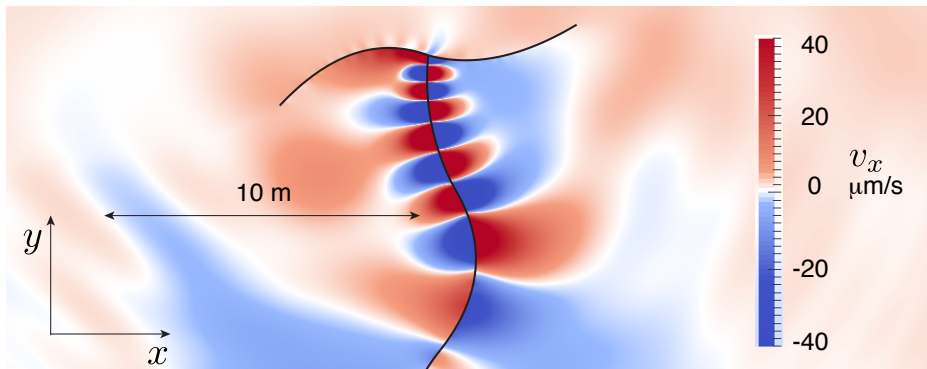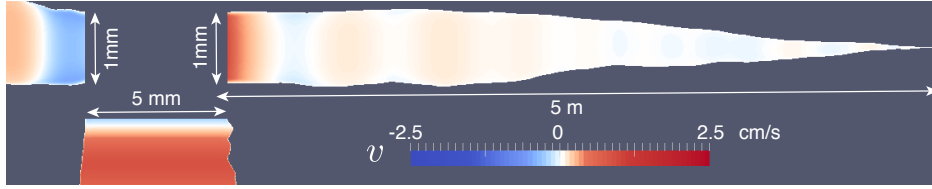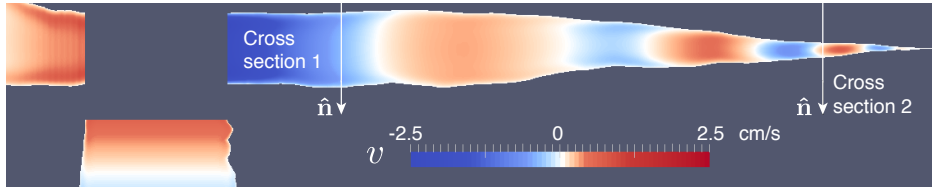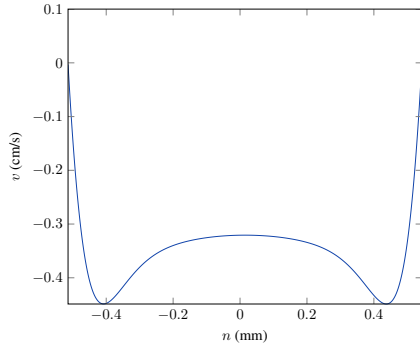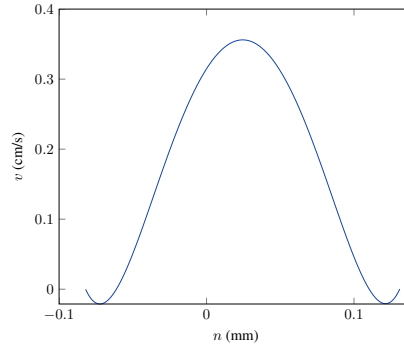

(a) $t = 26$ ms.

(b) $t = 50$ ms.

FIG. 5. *Snapshots in time of Krauklis waves propagating along a fluid-filled crack (solid line); color shows velocity in x direction. The discontinuity in color indicates opening/closing motions of the crack. 241×241 grid points per block.*

(a) $t = 26$ ms.

(b) $t = 50$ ms.

(c) Cross section 1.

(d) Cross section 2.

FIG. 6. *(a) and (b) Snapshots in time of fluid velocity field inside the main crack and branches. (c) and (d) Velocity profiles for the cross sections marked in (b). Note boundary layers and non-monotonic profiles, both characteristic of oscillatory flows at high frequency. 241 grid points along each crack segment and 241 grid points across the crack width.*

5.2.1. Excitation at the crack mouth. In this first problem, waves are excited by specifying a pressure boundary condition $p(0, t) = g(t)$ on Γ_1 (the bottom end of the main crack, referred to below as the crack mouth). Excitation at the crack mouth preferentially generates Krauklis waves that propagate along the cracks, ultimately leading to resonance at specific frequencies determined by the crack geometry. Crack mouth excitation can arise from pressure changes transmitted to the crack by an unmodeled narrow conduit or pipe, such as a well in hydraulic fracturing operations in an oil or gas reservoir. For more details on this problem class, see [26]. The boundary data is $g(t) = A \sin(\omega t) \exp(-\eta t)$, where $A = 100$ kPa, $\omega = 1.2 \times 10^5$ s^{-1}, and $\eta = 100$ s^{-1}. This function is a chirp with a maximum frequency $f_{max} \approx 2000$ Hz at 1% of peak amplitude. The maximum frequency f_{max} is used to estimate the minimum wavelength λ_{min} that needs to be resolved in the simulation. The relationship between wavelength λ and frequency f is determined by the dispersion

relation of the Krauklis waves propagating along the crack. For an infinitely long, planar crack filled with an inviscid fluid, we have [24]

$$\lambda = \left(2\pi \frac{Gw_0}{(1-\nu)\rho_f f^2}\right)^{1/3}.$$

We can then estimate $\lambda_{min} \sim \lambda(f_{max}) \sim 0.1$ m, suggesting that λ_{min} will be well-resolved on both the coarse and fine grids. To set the grid spacing in the n-direction within the fluid, we estimate the ratio of the boundary layer thickness to crack width as $\sqrt{\mu/(\rho_f \omega)}/\max w_0 \sim 10\%$, which should also be well-resolved on both the coarse and fine grids.

The pressure perturbation applied at the crack mouth excites Krauklis waves propagating along the fluid-filled crack (Figure 5). As Krauklis waves propagate along the crack, the crack walls oscillate inward and outward. A pair of counter-propagating waves are formed when the waves are partially reflected at the crack tips and the crack junction. Krauklis waves are attenuated primarily by viscous dissipation in the fluid, which in the wider parts of the crack is confined to boundary layers at the walls of the crack (Figure 6). The coarse and fine grid simulations are visually identical (not shown).

5.2.2. Excitation in the solid. This second problem, involving excitation in the solid, demonstrates the potential of our method for studying seismic wave scattering from fluid-filled cracks. Seismic waves in the solid can be excited by explosions or other active sources, or by naturally occurring impulsive perturbations such as small earthquakes (i.e., microseismic events). The latter, when the earthquakes are much smaller than modeled wavelengths, can be treated as point moment tensor sources. Details on how to discretize the singular source terms with high-order accuracy can be found in [37]. Here, for simplicity, we excite waves by specifying a Gaussian function as the initial condition in the solid: $v_x(x,y,0) = \exp\left(-\frac{1}{2a^2}(x - x_*)^2 - \frac{1}{2a^2}(y - y_*)^2\right)$ mm/s, where $a = 1/\sqrt{200} \approx 7.1$ cm and $(x_*, y_*) = (-1.5, -4)$ m with the origin located at the bottom end of Γ_1. All of the other solid and fluid fields are initially zero.
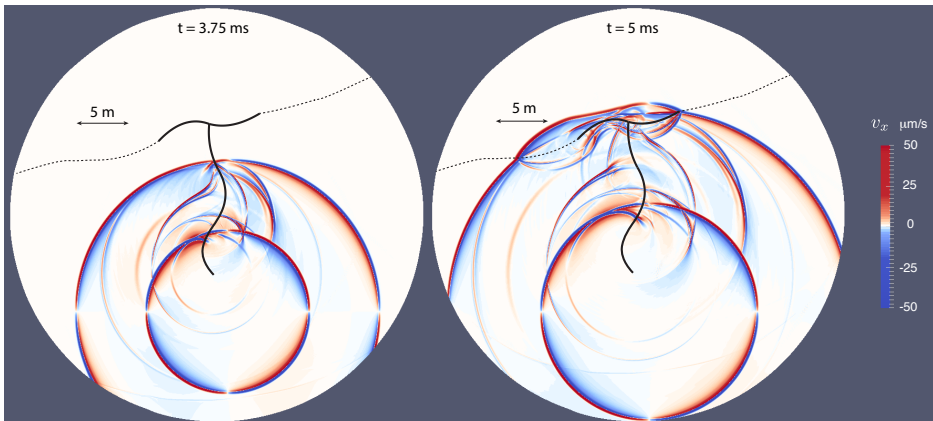

FIG. 7. *Snapshots in time of seismic wave scattering from a fluid-filled crack (solid line) and material interface (dashed line). 481×481 grid points per block.*

The initial disturbance excites both compressional (P) waves and shear (S) waves that scatter from the fluid-filled crack (Figure 7). P-to-S conversion along the crack
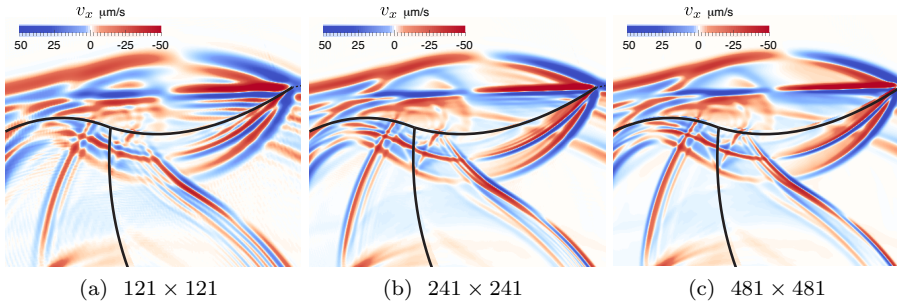
(a) 121×121 (b) 241×241 (c) 481×481

FIG. 8. *Grid refinement study at $t = 5$ ms (grid points per block listed listed in sub-captions).*

639 generates shear head waves, which have curved wavefronts due to the curvature of
640 the crack itself. All waves undergo reflections and additional mode conversations
641 upon reaching the branch segments (and material interface). Diffracted waves from
642 the crack junction are also evident. Note that in contrast to the previous problem,
643 Krauklis waves are almost absent. This is because excitation in this problem is from
644 a perturbation to particle velocity approximately normal to the main crack and with
645 symmetry across the crack. Opening or closing motions of the crack are therefore
646 negligible.
647   Figure 8 shows a zoomed-in version of the wavefield at the final time ($t = 5$ ms)
648 at three different grid resolutions. Dispersion errors that are evident on the coarsest
649 mesh vanish with refinement.
650   To investigate the computational cost of the fluid model, we compare the per-
651 formance of simulations with and without the fluid. In the simulation without the
652 fluid, we remove the fluid blocks and instead couple to the neighboring solid blocks
653 directly to one another. We measure the time to solution for both simulations after a
654 fixed number of time steps. The test is conducted on the grid with lowest resolution,
655 using 121×121 grid points per block in both the solid and fluid (when present). The
656 computational cost of the fluid is only about 8% of the total cost. This cost is slightly
657 less than the ratio of the number of fluid to solid blocks used in this test.

658   **6. Conclusions.** We have developed a method to simulate wave propagation
659 in and around cracks containing a viscous, compressible fluid. Our method achieves
660 computational efficiency relative to other commonly used methods through two key
661 components.
662   First, rather than solving the full linearized Navier-Stokes equations for the fluid,
663 we use a lubrication-type approximation of the fluid response. Viscous effects enter
664 only through one-dimensional diffusion operators in the direction spanning the crack
665 width. Even with this approximation, the semi-discrete system of equations can be
666 quite stiff, such that fully explicit time-stepping methods would require several orders
667 of magnitude smaller time steps than the time step required for explicit integration
668 of the elastic wave equation alone.
669   Second, the computational efficiency is enhanced by partitioning the semi-discrete
670 equations in conjunction with an implicit-explicit Runge-Kutta time-stepping method.
671 Specifically, we treat the elastic wave equation in the solid and the wave propagation
672 part of the fluid equations in a fully explicit manner, whereas the viscous (diffusion)
673 term and fluid-solid coupling terms in the fluid are treated in an implicit manner. By
674 enforcing the coupling conditions using characteristic variables, the overall system of

equations can be integrated using the maximum stable time step for wave propagation only. For typical fluid and solid properties, this corresponds to the typical CFL-limited time step used for explicit solution of the elastic wave equation.

Although we developed the numerical scheme in the context of high-order finite differences, the fluid model and many of the results related to the coupling formulation and partitioning should be applicable to other provably stable schemes with weakly enforced coupling conditions in SBP-SAT form (e.g., discontinuous Galerkin methods).

Finally, the method was applied to several application problems involving waves in and around fluid-filled cracks. Excitation at the crack mouth generates large amplitude Krauklis waves, and simulations like the ones shown in this work can be used to quantify Krauklis wave resonances and their relation to crack geometry [26]. The method can also be used to study scattering of seismic waves by fluid-filled cracks. Obvious applications include seismic imaging of fractured hydrocarbon-bearing reservoirs, crevasse systems in glaciers and ice sheets, and magmatic dike and sill complexes beneath active volcanoes.

Appendix A. Energy conserving penalty parameters.   This appendix continues Section 4.1 with a more detailed investigation of how the stability of the fully discrete approximation is influenced by how the coupling conditions are enforced. This is done by further investigation of the one-dimensional model problem (35), but with a different choice of penalty parameters. Specifically, we take $\alpha_s \to \infty$ and $\beta_s = 0$, for which (35) becomes

(41)
$$\int \phi_s \rho_s \frac{\partial v_x}{\partial t} dy = \int \phi_s \frac{\partial \sigma_{xy}}{\partial y} dy + \left[\phi_s \left(\sigma_{xy} - \tau \right) \right]_{y=0^+},$$
$$\int \varphi_s \frac{1}{G} \frac{\partial \sigma_{xy}}{\partial t} dy = \int \varphi_s \frac{\partial v_x}{\partial y} dy$$
$$\int \phi_f \rho_f \frac{\partial u}{\partial t} dn = \int \phi_f \tau \, dn - \left[\mu \frac{\partial \phi_f}{\partial n} \left(u - v_x \right) \right]_{n=w_0^+}.$$

The fluid traction is enforced as a Neumann condition on the solid and the solid velocity is enforced as a Dirichlet condition on the fluid. This way of enforcing the coupling conditions is a very common approach in many fluid-structure interaction schemes [19]. A consequence of using (41) is that there is no additional numerical energy dissipation:

(42)
$$\frac{1}{2} \frac{d}{dt} \left(\int \rho_s v_x^2 + \frac{1}{G} \sigma_{xy}^2 dy + \int \rho_f u^2 dn \right) = - \int \frac{\tau^2}{\mu} dn.$$

We next investigate the impact of this coupling procedure on the semi-discrete and fully discrete approximations of (41). We write the semi-discrete approximation of (41) in the strong form:

(43)
$$\frac{dq}{dt} = (W + C)q,$$

where $q = [v_x^T \; \sigma_{xy}^T \; u^T]^T$. We use the partitioning $dq/dt = (F^{EX} + F^{IM})q$, with $F^{EX} = W^{EX} + C^{EX}$ and $F^{IM} = W^{IM} + C^{IM}$. Consider the following choice of the partitioning:

$$W^{EX} = \begin{bmatrix} 0 & D_y/\rho_s & 0 \\ GD_y & 0 & 0 \\ 0 & 0 & 0 \end{bmatrix}, \; W^{IM} = \begin{bmatrix} 0 & 0 & 0 \\ 0 & 0 & 0 \\ 0 & 0 & \mu/\rho_f D_n D_n \end{bmatrix},$$

(44)
$$C^{EX} = \begin{bmatrix} 0 & H_y^{-1} L_s L_s^T & -\mu H_y^{-1} L_s L_f^T D_n \\ 0 & 0 & 0 \\ 0 & 0 & 0 \end{bmatrix},$$

$$C^{IM} = \frac{\mu}{\rho_f} \begin{bmatrix} 0 & 0 & 0 \\ 0 & 0 & 0 \\ H_n^{-1} D_n^T L_f L_s^T & 0 & -H_n^{-1} D_n^T L_f L_f^T \end{bmatrix}.$$

For simplicity, the grid spacing is uniform, implying that there are no metric coefficients. This partitioning is the same as the one we used before; see (32). The solid is fully explicit and the fluid is fully implicit (because in this one-dimensional problem there is no wave propagation in the fluid).
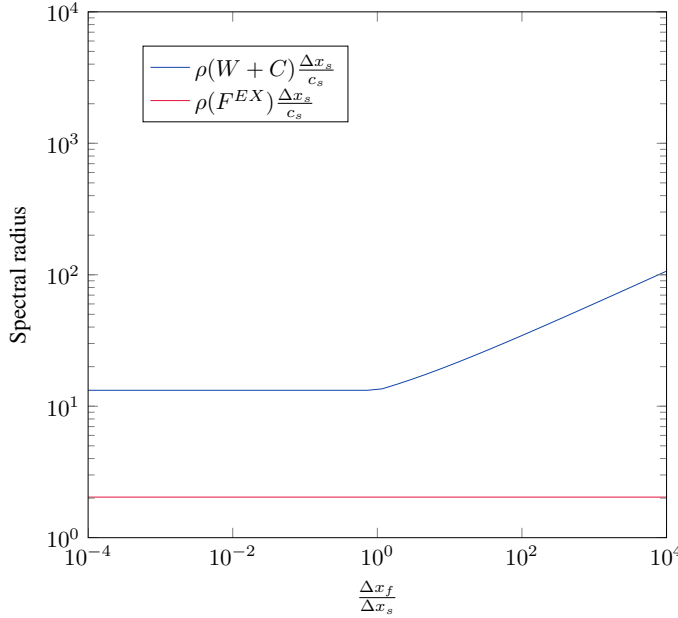

FIG. 9. *Spectral radii of the semi-discrete approximation of the problem (41). The spectral radii $\rho(W + C)$ (complete problem) and $\rho(F^{EX})$ (explicit part of the semi-discrete approximation) are shown.*

Next, we compute the spectral radius of the semi-discrete approximation while varying $\Delta x_f / \Delta x_s$. As in Section 4.1, we use $\rho_s = \rho_f$ and discretize using the SBP(6,3) operators. However, for this new choice of penalty parameters, Figure 9 shows that the spectral radius $\rho(W + C)$ is at about one order of magnitude larger than the spectral radius $\rho(F^{EX})$ (which is determined by the explicit part of the semi-discrete approximation, i.e., by wave propagation). Note that the spectral radius of the explicit part $\rho(F^{EX})$ does not change as $\Delta x_f / \Delta x_s$ is varied, indicating that there is no source
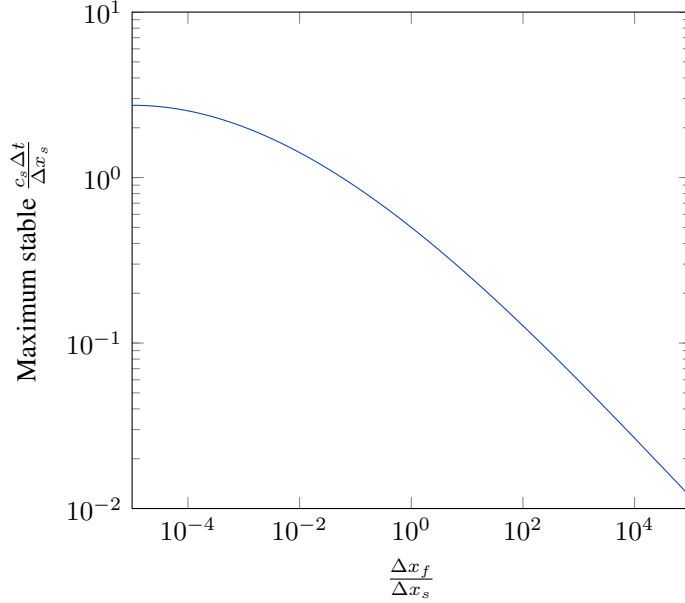
FIG. 10. *Maximum stable CFL number of the fully discrete scheme approximating the problem (41) with partitioning (44).*

of stiffness in the explicit part. However, when we look at the maximum stable time step of the fully discrete approximation, we find that it is necessary to decrease the time step for stability (Figure 10). The important lesson here is that this choice of the penalty parameters, when used in combination with the partitioning (44), causes the scheme to be unstable for sufficiently large $\Delta x_f/\Delta x_s$, unless the time step is decreased. In contrast, the scheme is stable for the penalty parameter choice presented in Section 4.1 regardless of the value of $\Delta x_f/\Delta x_s$.

Another way to stabilize the scheme (41), without changing the penalty parameters, is to modify the partitioning. This modification should be done such that energy is conserved in the fully discrete approximation as well. Consider the following energy conservative partitioning:

$$(45) \qquad C^{EX} = \begin{bmatrix} 0 & H_y^{-1} L_s L_s^T & 0 \\ 0 & 0 & 0 \\ 0 & 0 & 0 \end{bmatrix},$$

$$C^{IM} = \begin{bmatrix} 0 & 0 & -\mu/\rho_s H_y^{-1} L_s L_f^T D_n \\ 0 & 0 & 0 \\ \mu/\rho_f H_n^{-1} D_n^T L_f L_s^T & 0 & -\mu/\rho_f H_n^{-1} D_n^T L_f L_f^T \end{bmatrix}.$$

In this case, one can easily show that each sub-problem satisfies an energy balance, implying $\langle q, F^{EX} q \rangle \leq 0$ and $\langle q, F^{IM} q \rangle \leq 0$, where $\langle u, v \rangle = \sum u_j v_j h$ is the discrete inner-product, i.e., F^{EX} and F^{IM} are both semi-bounded. We again obtain a fully discrete scheme with the attractive property that the maximum stable time step is set by wave propagation. In practice, however, we do not use this partitioning because the solid penalty terms are treated implicitly, making it more difficult to implement.

REFERENCES

[1] U. M. Ascher, S. J. Ruuth, and R. J. Spiteri, *Implicit-explicit Runge-Kutta methods for time-dependent partial differential equations*, Appl. Num. Math., 25 (1997), pp. 151–167, doi:10.1016/s0168-9274(97)00056-1.

[2] N. Balmforth, C. Cawthorn, and R. Craster, *Contact in a viscous fluid. part 2. a compressible fluid and an elastic solid*, J. Fluid Mech., 646 (2010), pp. 339–361, doi:10.1017/s0022112009993168.

[3] G. K. Batchelor, *An introduction to fluid dynamics*, Cambridge university press, 2000, doi:10.1017/cbo9780511800955.001.

[4] M. Calvo, J. de Frutos, and J. Novo, *Linearly implicit Runge-Kutta methods for advection-reaction-diffusion equations*, Appl. Num. Math., 37 (2001), pp. 535 – 549, doi:10.1016/S0168-9274(00)00061-1.

[5] M. Carpenter, D. Gottlieb, and S. Abarbanel, *Time-stable boundary conditions for finite-difference schemes solving hyperbolic systems: methodology and application to high-order compact schemes*, J. Comput. Phys., (1993), doi:10.1006/jcph.1994.1057.

[6] T. Chen, M. Fehler, X. Fang, X. Shang, and D. Burns, *Sh wave scattering from 2-d fractures using boundary element method with linear slip boundary condition*, Geophys. J. Int., 188 (2012), pp. 371–380, doi:10.1190/1.3627802.

[7] B. Chouet, *Dynamics of a fluid-driven crack in three dimensions by the finite difference method*, J. Geophys. Res.: Solid Earth, 91 (1986), pp. 13967–13992, doi:10.1029/jb091ib14p13967.

[8] B. Chouet and B. R. Julian, *Dynamics of an expanding fluid-filled crack*, J. Geophys. Res.: Solid Earth, 90 (1985), pp. 11187–11198, doi:10.1029/jb090ib13p11187.

[9] R. T. Coates and M. Schoenberg, *Finite-difference modeling of faults and fractures*, Geophys., 60 (1995), pp. 1514–1526, doi:10.1190/1.1443884.

[10] O. Coutant, *Numerical study of the diffraction of elastic waves by fluid-filled cracks*, J. Geophys. Res.: Solid Earth, 94 (1989), pp. 17805–17818, doi:10.1029/jb094ib12p17805.

[11] K. Duru and E. M. Dunham, *Dynamic earthquake rupture simulations on nonplanar faults embedded in 3d geometrically complex, heterogeneous elastic solids*, J. Comput. Phys., 305 (2016), pp. 185–207, doi:10.1016/j.jcp.2015.10.021.

[12] C. Farhat, M. Lesoinne, and P. Le Tallec, *Load and motion transfer algorithms for fluid/structure interaction problems with non-matching discrete interfaces: Momentum and energy conservation, optimal discretization and application to aeroelasticity*, Comput. Methods Appl. Mech. Engr., 157 (1998), pp. 95–114, doi:10.1016/s0045-7825(97)00216-8.

[13] V. Ferrazzini and K. Aki, *Slow waves trapped in a fluid-filled infinite crack: implication for volcanic tremor*, J. Geophys. Res., 92 (1987), pp. 9215–9223, doi:10.1029/jb092ib09p09215.

[14] M. Frehner and S. M. Schmalholz, *Finite-element simulations of stoneley guided-wave reflection and scattering at the tips of fluid-filled fractures*, Geophys., 75 (2010), pp. T23–T36, doi:10.1190/1.3340361.

[15] B. Froehle and P.-O. Persson, *A high-order discontinuous Galerkin method for fluid–structure interaction with efficient implicit–explicit time stepping*, J. Comput. Phys., 272 (2014), pp. 455–470, doi:10.1016/j.jcp.2014.03.034.

[16] J. Groenenboom and J. Falk, *Scattering by hydraulic fractures: Finite-difference modeling and laboratory data*, Geophys., 65 (2000), pp. 612–622, doi:10.1190/1.1444757.

[17] G. Guidoboni, R. Glowinski, N. Cavallini, and S. Canic, *Stable loosely-coupled-type algorithm for fluid–structure interaction in blood flow*, J. Comput. Phys., 228 (2009), pp. 6916–6937, doi:10.1016/j.jcp.2009.06.007.

[18] Y. Hori, *Hydrodynamic lubrication*, Springer Science & Business Media, 2006, doi:10.1007/4-431-27901-6.

[19] G. Hou, J. Wang, and A. Layton, *Numerical methods for fluid-structure interaction a review*, J. Commun. Phys., 12 (2012), pp. 337–377, doi:10.4208/cicp.291210.290411s.

[20] C. A. Kennedy and M. H. Carpenter, *Additive Runge-Kutta schemes for convection-diffusion-reaction equations*, Appl. Num. Math., 44 (2003), pp. 139 – 181, doi:10.1016/S0168-9274(02)00138-1.

[21] V. Korneev, *Slow waves in fractures filled with viscous fluid*, Geophys., 73 (2007), pp. N1–N7, doi:10.1190/1.2802174.

[22] J. E. Kozdon, E. M. Dunham, and J. Nordström, *Interaction of waves with frictional interfaces using summation-by-parts difference operators: Weak enforcement of nonlinear boundary conditions*, J. Sci. Comput., 50 (2012), pp. 341–367, doi:10.1007/s10915-011-9485-3.

[23] J. E. Kozdon, E. M. Dunham, and J. Nordström, *Simulation of dynamic earthquake rup-

813   *tures in complex geometries using high-order finite difference methods*, J. Sci. Comput., 55
814   (2013), pp. 92–124, doi:10.1007/s10915-012-9624-5.
815   [24] P. KRAUKLIS, *On some low-frequency vibrations of a liquid layer in an elastic medium*, J. Appl.
816   Math. Mech., 26 (1962), pp. 1685–1692, doi:10.1016/0021-8928(62)90203-4.
817   [25] H. KREISS AND G. SCHERER, *Finite element and finite difference methods for hyperbolic partial
818   differential equations*, Academic Press, 1974, doi:10.1016/b978-0-12-208350-1.50012-1.
819   [26] C. LIANG, O. O'REILLY, E. M. DUNHAM, AND D. MOOS, *Hydraulic fracture diagnostics from
820   krauklis wave resonance and tube wave reflections*, Geophys., (2016). In review.
821   [27] B. P. LIPOVSKY AND E. M. DUNHAM, *Vibrational modes of hydraulic fractures: Inference
822   of fracture geometry from resonant frequencies and attenuation*, J. Geophys. Res.: Solid
823   Earth, doi:10.1002/2014jb011286.
824   [28] V. D. LISEIKIN, *Grid generation methods*, Springer Science & Business Media, 2009,
825   doi:10.1007/978-90-481-2912-6.
826   [29] R. LÖHNER, C. YANG, J. CEBRAL, J. D. BAUM, H. LUO, D. PELESSONE, AND C. CHARMAN,
827   *Fluid-structure-thermal interaction using a loose coupling algorithm and adaptive unstruc-
828   tured grids*, in Proc., 29th AIAA Fluid Dynamics Conference, 1998, doi:10.2514/6.1998-
829   2419.
830   [30] K. MATTSSON, *Summation by parts operators for finite difference approximations of
831   second-derivatives with variable coefficients*, J. Sci. Comput., 51 (2012), pp. 650–682,
832   doi:10.1007/s10915-011-9525-z.
833   [31] V. MIRYAHA, A. SANNIKOV, AND I. B. PETROV, *Discontinuous Galerkin method for numerical
834   simulation of dynamic processes in solids*, Mathematical Models and Computer Simula-
835   tions, 7 (2015), pp. 446–455, doi:10.1134/s2070048215050087.
836   [32] J. NEUBERG, R. LUCKETT, B. BAPTIE, AND K. OLSEN, *Models of tremor and low-frequency
837   earthquake swarms on montserrat*, J. Volcanol. Geotherm. Res., 101 (2000), pp. 83–104,
838   doi:10.1016/s0377-0273(00)00169-4.
839   [33] J. NORDSTRÖM, *Conservative finite difference formulations, variable coefficients, en-
840   ergy estimates and artificial dissipation*, J. Sci. Comput., 29 (2006), pp. 375–404,
841   doi:10.1007/s10915-005-9013-4.
842   [34] J. NORDSTRÖM, *A roadmap to well posed and stable problems in computational physics*, J. Sci.
843   Comput., (2016). Accepted.
844   [35] P. OLSSON, *Summation by parts, projections, and stability*, Math. Comput., 64 (1995),
845   pp. 1035–1035, doi:10.2307/2153482.
846   [36] L. PARESCHI AND G. RUSSO, *Implicit-explicit Runge-Kutta schemes and applications
847   to hyperbolic systems with relaxation*, J. Sci. Comput., 25 (2005), pp. 129–155,
848   doi:10.1007/bf02728986, 10.1007/bf02728986.
849   [37] N. A. PETERSSON, O. O'REILLY, B. SJÖGREEN, AND S. BYDLON, *Discretizing singular point
850   sources in hyperbolic wave propagation problems*, J. Comput. Phys., 321 (2016), pp. 532–
851   555, doi:10.1016/j.jcp.2016.05.060.
852   [38] S. PIPERNO, *Explicit/implicit fluid/structure staggered procedures with a structural predic-
853   tor and fluid subcycling for 2d inviscid aeroelastic simulations*, Int. J. Num. Methods
854   Fluids, 25 (1997), pp. 1207–1226, doi:10.1002/(sici)1097-0363(19971130)25:10¡1207::aid-
855   fld616¿3.0.co;2-r.
856   [39] T. POINTER, E. LIU, AND J. A. HUDSON, *Numerical modelling of seismic waves scattered by
857   hydrofractures: application of the indirect boundary element method*, Geophys. J. Int., 135
858   (1998), pp. 289–303, doi:10.1046/j.1365-246x.1998.00644.x.
859   [40] P. J. ROACHE, *Code verification by the method of manufactured solutions*, J. Fluids Eng., 124
860   (2002), pp. 4–10, doi:10.1115/1.1436090.
861   [41] B. STERNLICHT AND O. PINKUS, *Theory of Hydrodynamic Lubrication*, McGraw-Hill, New York,
862   1961.
863   [42] B. STRAND, *Summation by parts for finite difference approximations for d/dx*, J. Comput.
864   Phys., 110 (1994), pp. 47–67, doi:10.1006/jcph.1994.1005.
865   [43] M. SVÄRD AND J. NORDSTRÖM, *On the order of accuracy for difference approxima-
866   tions of initial-boundary value problems*, J. Comput. Phys., 218 (2006), pp. 333–352,
867   doi:10.1016/j.jcp.2006.02.014.
868   [44] M. SVÄRD AND J. NORDSTRÖM, *Review of summation-by-parts schemes for initial–boundary-
869   value problems*, J. Comput. Phys., 268 (2014), pp. 17–38, doi:10.1016/j.jcp.2014.02.031.
870   [45] G. TAYLOR, *Effects of compressibility at low reynolds number*, J. Aeronaut. Sci., (1957),
871   doi:10.2514/8.3906.
872   [46] A. H. VAN ZUIJLEN AND H. BIJL, *Implicit and explicit higher order time integration schemes
873   for structural dynamics and fluid-structure interaction computations*, Comput. Struct., 83
874   (2005), pp. 93–105, doi:10.1016/j.compstruc.2004.06.003.

[47] C. Wu, J. M. Harris, K. T. Nihei, and S. Nakagawa, *Two-dimensional finite-difference seismic modeling of an open fluid-filled fracture: Comparison of thin-layer and linear-slip models*, Geophys., 70 (2005), pp. T57–T62, doi:10.1190/1.1988187.

[48] M. Yamamoto and H. Kawakatsu, *An efficient method to compute the dynamic response of a fluid-filled crack*, Geophys. J. Int., 174 (2008), pp. 1174–1186, doi:10.1111/j.1365-246x.2008.03871.x.

2. Crack junction coupling conditions. Consider the coupling of three cracks at a junction. Prior to weakly enforcing the coupling conditions, the work rate at the junction is

$$\frac{dE}{dt} = -\sum_{i=1}^{3} n^{(i)} w_0^{(i)} \hat{p}^{(i)} \hat{\dot{u}}^{(i)} - \mathcal{R},$$

where (i) labels each crack. We use $n^{(i)}$ to keep track of the sign at each end ($n^{(i)} = -1$ and $n^{(i)} = 1$ for the left and right end, respectively). While the crack can be in any direction, the left end is defined at the minimum arc length s along the crack. At the junction, the pressure is continuous: $\hat{p} = \hat{p}^{(1)} = \hat{p}^{(2)} = \hat{p}^{(3)}$. Mass conservation, in the context of our linearized model, requires

(46)
$$\sum_{i=1}^{3} n^{(i)} \rho_f^{(i)} w_0^{(i)} \hat{\dot{u}}^{(i)} = 0.$$

To ensure $\mathcal{R} \geq 0$, we need

(47)
$$\alpha^{(i)} n^{(i)} w_0^{(i)} \hat{\dot{u}}^{(i)} + \hat{p} = \alpha^{(i)} n^{(i)} w_0^{(i)} \bar{v}^{(i)} + p^{(i)}, \text{ for } i = 1, 2, 3.$$

Multiplying (47) by $\rho_f^{(i)} \alpha^{(i+1)} \alpha^{(i+2)}$, and cyclically summing over $i = 1, 2, 3$ results in

$$\sum_{j=1}^{3} \alpha^{(j)} \sum_{i=1}^{3} n^{(i)} \rho_f^{(i)} w_0^{(i)} \hat{\dot{u}}^{(i)} + \sum_{i=1}^{3} \rho_f^{(i)} w_0^{(i)} \sum_{j \neq i} \alpha^{(j)} \hat{p} = \zeta.$$

where $\zeta = \sum_{i=1}^{3} \rho_f^{(i)} w_0^{(i)} p^{(i)} \sum_{j \neq i} \alpha^{(j)} + \sum_{i=1}^{3} w_0^{(i)} n^{(i)} v^{(i)} \sum_{j=1}^{3} \alpha^{(j)}$. Finally, using (46) results in

$$\hat{p} = \frac{\zeta}{\sum_{i=1}^{3} \rho_f^{(i)} w_0^{(i)} \sum_{j \neq i} \alpha^{(j)}}, \quad \hat{\dot{u}}^{(i)} = \bar{u}^{(i)} + \frac{p^{(i)} - \hat{p}}{\alpha^{(i)} n^{(i)} w_0^{(i)}}.$$